This is a preprint, the final version is subject to change, of the American Mineralogist (MSA)
Cite as Authors (Year) Title. American Mineralogist, in press.
DOI: https://doi.org/10.2138/am-2019-6966

Revision 1

Thermoelasticity, cation exchange and deprotonation in Fe-rich holmquistite: towards a crystal-chemical model for the high-temperature behavior of orthorhombic amphiboles

ROBERTA OBERTI[1,*], MASSIMO BOIOCCHI[2], MICHELE ZEMA[1,3]

[1] CNR-Istituto di Geoscienze e Georisorse, Sede secondaria di Pavia, via Ferrata 1, 27100 Pavia, Italy

[2] Centro Grandi Strumenti, Università di Pavia, via Bassi 21, 27100 Pavia, Italy

[3] Dipartimento di Scienze della Terra e dell'Ambiente, Università di Pavia, via Ferrata 1, 27100 Pavia, Italy

* email: oberti@crystal.unipv.it

ABSTRACT

The thermoelastic behavior of a crystal of Fe-rich holmquistite with crystal-chemical formula $^{A}(K_{0.01}Na_{0.01})^{B}(Li_{1.88}Mg_{0.10}Na_{0.02})^{C}(Mg_{1.68}Fe^{2+}_{1.42}Mn^{2+}_{0.02}Al_{1.88})^{T}Si_{8.00}\,O_{22}{}^{W}[(OH)_{1.97}F_{0.03}]$ was studied by single-crystal X-ray diffraction to 1023 K, where isothermal annealing in air for 160

This is a preprint, the final version is subject to change, of the American Mineralogist (MSA)
Cite as Authors (Year) Title. American Mineralogist, in press.
DOI: https://doi.org/10.2138/am-2019-6966

hours yielded the loss of 0.85 H *apfu* coupled with oxidation of ^{M1}Fe. A complex pattern of cations exchanges was deciphered by comparing structure refinements done before and after annealing. Li migration from the *M*4 to the *M*3 site is responsible for non-linearity of the *c* parameter around 600 K during the first annealing. Cooling of the partially deprotonated crystal to R*T* showed discontinuities in trends of the *b* and *c* parameters around 820-800 K, which cannot be ascribed to a phase transition and must be explained by a rearrangement of the structural units affecting the geometry of the *M*4 polyhedron. Such discontinuities have never been observed in amphiboles before and must be related to dimensional constraints deriving from the peculiar composition of this amphibole, which contains the smallest possible homovalent constituents, i.e., ^{B}Li, ^{C}Al and ^{T}Si. The calculated thermoelastic parameters are: Fe-rich holmquistite: $\alpha_a = 1.36(2)\times10^{-5}$; $\alpha_b = 0.55(1)\times10^{-5}$; $\alpha_c = 1.5(1)\times10^{-5} - 6.7(9)\times10^{-9}$; $\alpha_V = 3.5(3)\times10^{-5} - 0.8(3)\times10^{-8}$ (polynomial); $2.58(6)\times10^{-5}$ (linear); partially deprotonated Fe-rich holmquistite: $\alpha_a = 1.324(9)\times10^{-5}$ (R*T*-1023 K); $\alpha_b = 0.60(1)\times10^{-5}$ (R*T*-773 K); $\alpha_c = 0.68(2)\times10^{-5}$ (R*T*-773 K); $\alpha_V = 2.59(2)\times10^{-5}$ (R*T*-773 K). Fe-rich holmquistite is much stiffer than all the previously studied orthorhombic *Pnma* and *Pnmn* amphiboles. The results of this work allow progress towards a general model able that will explain how the amphibole structure reacts to non-ambient conditions, and allows the release of water in diverse geological situations.

Keywords Amphibole - Holmquistite - H*T* behavior - Thermoelasticity - Deprotonation - Structure refinement

INTRODUCTION

Hydrous minerals with topologically complex structure and crystal-chemistry, such as amphibole, mica, serpentine, tourmaline, have a complex behavior under increasing *T* and *P*. The most relevant phenomena observed are expansion of the unit cell (often anisotropic), cation disordering among sites with similar or different coordination, phase transitions and deprotonation coupled with iron oxidation. All these processes significantly affect cation order, molar volume and

thermoelasticity in the studied phase. The reasons why and how deprotonation occurs is crucial to model the release of water in some geological setting, such as during subduction or degassing during ascent of magma in volcanic conduits.

Crystallographic studies concerning the evolution of the structure with *T* have been done so far for amphiboles (after the review by Welch et al. 2007, see: Della Ventura et al. 2015, 2018a,b; Oberti et al. 2009, 2011, 2016, 2018; Welch et al. 2011a,b; Zema et al. 2012) and micas (Ventruti et al. 2008; Zema et al. 2010). Studies of the oxidation/deprotonation process based upon vibrational spectroscopic evidences are also available for tourmalines (Fuchs et al. 2002; Pieczka and Kraczka 2004; Bačik et al. 2011; Filip et al. 2012; Bosi et al. 2016a,b) but do not provide information on thermal expansivity. For serpentine, the loss of water has been monitored by TEM and spectroscopic techniques (Gualtieri et al. 2012; Trittschack and Grobéty 2012, 2013).

Amphiboles are an important family of rock-forming minerals with a complex crystal-chemistry. However, their compositional diversity gives them potential as sensitive monitors of petrological processes; therefore, H*T* studies of amphiboles under controlled conditions are being systematically done to confirm our present knowledge on cation ordering and exchange vectors (which is mostly derived from crystal-chemical and petrological observations on many compositions from different localities and geological environments) and to provide key information for petrogenetic studies. Indeed, H*T* studies of amphiboles can provide precious information on phase stability, molar volumes and crystal-chemical markers to be used in thermodynamic modelling in upper-mantle geological contexts, as well as on the conditions of hydrogen release and thus on the hydrogen/water budget in the Earth mantle. This last issue is becoming more and more important, because it is not only related to plate tectonics but also to Earth's climate and habitability (cf. for instance Yang et al. (2016) and references therein).

We have already examined the high-temperature and high-pressure behavior of two compositions of the orthorhombic magnesium-iron- manganese amphibole subgroup by single-crystal X-ray diffraction (SC-XRD): anthophyllite (ideally $^{A}\square^{B}Mg_2{}^{C}Mg_5{}^{T}Si_8O_{22}{}^{W}(OH)_2$; Welch et

This is a preprint, the final version is subject to change, of the American Mineralogist (MSA)
Cite as Authors (Year) Title. American Mineralogist, in press.
DOI: https://doi.org/10.2138/am-2019-6966

al. 2011a,b) and gedrite (ideally $^{A}Na^{B}Mg_2{}^{C}(Mg_4Al)^{T}(Si_6Al_2)O_{22}{}^{W}(OH)_2$ but always occurring with significant ^{A}Na and ^{C}Fe contents; Zema et al. 2012; Nestola et al. 2012). For proto-ferro-suenoite (ideally $^{A}\square{}^{B}Mn^{2+}{}_2{}^{C}Mg_5{}^{T}Si_8O_{22}{}^{W}(OH)_2$ but occurring with a different symmetry, i.e. *Pnmn*), only R*T* (Sueno et al. 2002) and HP data (Zanazzi et al. 2010) are available. Note that in the present scheme for amphibole nomenclature and classification (Hawthorne et al. 2012) A, B, C and T refers to the cations occurring at the *A* (*A*, *Am*, *A*2), *M*4, *M*1-3,*T*1-2 sites, respectively, and W refers to anions occurring at the O3 site (cf. Figure 1 for site identification). For monoclinic amphiboles, the use of parentheses, such as in *M*(4), is required.

We now report on the H*T* behavior of the third composition of reference for orthorhombic *Pnma* amphiboles, holmquistite (ideally $^{A}\square{}^{B}Li_2{}^{C}(Mg_3Al_2)^{T}Si_8O_{22}{}^{W}(OH)_2$). Holmquistite is unusual among amphiboles in that (i) the *A* site is empty (and hence more compressible and less expansible); (ii) the two independent double-chains of tetrahedra are occupied by the smallest possible T cation (Si), and (iii) they have to match with a strip built by three independent octahedra (*M*1, *M*2 and *M*3), one of which (*M*2) is almost fully occupied by the smallest possible trivalent C cation (Al); (iv) the structural units are connected by an *M*4 site occupied by the smallest monovalent B cation (Li). The presence of the smallest possible cations in all the structural sites is likely to determine important crystal-chemical constraints making the incorporation of large cations more difficult than in other amphibole positions. Indeed, ferro-holmquistite (the composition with Fe^{2+} dominant among C cations) occurs rarely (Cámara and Oberti 2005). Because the presence of Fe^{2+} is required to allow the loss of hydrogen (for recent and conclusive work on the mechanism of this process cf. Della Ventura et al. 2018a,b), we have chosen to examine a Fe-rich holmquistite in order to allow quantification of the effects of both thermal expansion and deprotonation upon holmquistite.

EXPERIMENTAL

Sample: provenance and composition

The crystals used for this study come from the holotype specimen of ferro-holmquistite (Cámara and Oberti 2005) found in the Greenbushes lithian pegmatite, Western Australia, 220 km south of Perth. The sample code 3380B (in the collection of Renato and Adriana Pagano) is used throughout this paper. The Greenbushes zoned pegmatite is one of the world largest producers of tantalum and lithium; the main body has sharply bounded Li-rich, K-rich, and Na-rich zones, the Na-rich zone being in the core. A review of the geology, mineralization, and geochronology of the Greenbushes pegmatite can be found in Partington et al. (1995) and references therein. Associated minerals include albite, quartz, biotite, tourmaline, garnet, tin with tantalite inclusions, zircon, and scapolite (Partington et al. 1995). Holmquistite formed because of lithium migration from the pegmatite into the amphibolite (Frost et al. 1987). It belongs to a late stage and replaces hornblende.

Characterization of the sample by Electron MicroProbe (EMP) analyses and single-crystal structure refinement gave a crystal-chemical formula of $^{A}(K_{0.01}Na_{0.01})\ ^{B}(Li_{1.88}Mg_{0.08}Na_{0.03}Fe^{2+}_{0.01})\ ^{C}(Al_{1.89}Fe^{2+}_{1.70}Mg_{1.39}Mn^{2+}_{0.02})^{T}Si_{8.00}O_{22}{}^{W}[(OH)_{1.97}F_{0.03}]$ for the holotype crystal and is described by Cámara and Oberti (2005). In that work, the Fe^{2+}/Mg ratio was shown to vary in different crystals from the same sample, which coupled with variations in the measured site-scattering values refined at the *M*1-3 sites and in the length of the *b* edge. Relative to the original ferro-holmquistite crystal studied by Cámara and Oberti (2005), the results of the structure refinement of the crystal used for the present work (3380B n. 7) are displaced by 0.34 *apfu* (atoms per formula unit) $^{C}Fe^{2+}_{-1}\ ^{C}Mg_{1}$ corresponding to a refined site-scattering for the C cations 4.7 electron per formula unit (*epfu*) lower (82.45 *epfu* for crystal n. 7 vs. 87.17 *epfu*. This is the only significant compositional difference observed, and the refined values of site scattering and mean bond-lengths at the individual sites indicate that this exchange occurs mostly at the *M*1 and *M*3 sites (*M*1: 35.44 *epfu and* 2.096 Å, *M*3: 18.97 *epfu* and 2.097 Å in crystal n. 7; *M*1: 37.82 *epfu* and 2.100 Å, *M*3: 20.63 *epfu* and 2.102 Å in Cámara and Oberti 2005), whereas those refined for the *M*2 (28.04 *epfu* and 1.931 Å for crystal n. 7; 28.72 *epfu* and 1.930 Å in Cámara and Oberti 2005) and the *M*4 (6.70 for crystal n. 7 vs. 7.2 e*pfu*) and T sites are more similar. This evidence suggests a composition very close to $^{A}(K_{0.01}$

This is a preprint, the final version is subject to change, of the American Mineralogist (MSA)
Cite as Authors (Year) Title. American Mineralogist, in press.
DOI: https://doi.org/10.2138/am-2019-6966

$Na_{0.01}$) $^{B}(Li_{1.88}Mg_{0.10}Na_{0.02})$ $^{C}(Mg_{1.68}Fe^{2+}_{1.42}Mn^{2+}_{0.02}Al_{1.88})$ $^{T}Si_{8.00}$ O_{22} $^{W}[(OH)_{1.97}F_{0.03}]$, and places the crystal studied in this work in the compositional field of holmquistite (because $^{C}Mg > {}^{C}Fe^{2+}$; Hawthorne et al. 2012). A sketch of the holmquistite structure and site nomenclature are given in Figure 1.

Single-crystal XRD analysis (in the *T* range 298-1023 K)

Experimental procedures are the same as those reported in previous studies of orthorhombic amphiboles (Welch et al. 2011a; Zema et al. 2012), and repeated here for the sake of completeness. Before annealing, crystals were mounted on glass fibers, and an ambient data set was collected for structure refinement on a Bruker AXS CCD diffractometer (operating condition in the next paragraph) in order to check for the presence of twins, inclusions or zones with bad crystal quality. Measurements of unit-cell parameters and intensity data collections at H*T* were done on a Philips PW1100 diffractometer operating with MoKα radiation at 30 mA/55 kV and using a 0.8 mm collimator. For the H*T* experiment, crystals were loaded into a 0.5 mm diameter quartz capillary and carefully positioned and secured at the sealed tip of the tube by packing with quartz-glass wool. The capillary was then attached to a Huber goniometer head and mounted on the diffractometer. The crystal was aligned optically, and a resistance heater was then placed around it in such a way that the assembly allowed for the incident and diffracted beams to reach and leave the crystal, passing through a kapton window. Geometrical restrictions allowed for the collection of diffracted beam up to ±28° in ω. The furnace was powered by a control unit equipped with a Eurotherm temperature controller, and temperature measured by a K-type thermocouple. Temperature was previously calibrated against the melting points of standard compounds (see, for example, Welch et al. 2011a) and by using the thermal expansion of quartz across the α–β phase transition (a quartz sphere of 0.3 mm diameter). Reported temperatures are precise to within ±5 K.

Unit-cell parameters

At each working temperature, the orientation matrix was updated by centering 24 reflections selected in the range $8< \theta <24°$, and then accurate lattice parameters were obtained by a least-squares procedure based on a locally modified version of the Philips LAT routine over 47–55 d^*_{hkl}, each measured from the positions of all reflection pairs *h, k*, *l* and *-h, -k*, *-l* in the range $3< \theta <26°$ (Cannillo et al. 1983). An explorative experiment was done on a crystal fragment of 0.78 × 0.64 × 0.33 mm^3 (3380B n. 4). Anomalies in thermal expansion, such as non-linear behavior of the *c* parameter, were observed from 623 K, and evidence of the onset of deprotonation was observed at 973 K. Isothermal annealing at 1073 K for two days yielded the expected decreases in the unit-cell parameters associated with deprotonation. In order to check whether or not deprotonation was complete, annealing to 1173 K was attempted, but the crystal quality deteriorated quickly. This behavior was different from what observed for other orthorhombic and monoclinic amphiboles with different compositions, which could be annealed up to 1273 K without deterioration. A crystal fragment of 0.20 × 0.35 × 0.55 mm^3 (3380B n. 7) was annealed up to 973 K at steps of 50 K (upward triangles in Figure 2). In order to check whether or not the non-linear behavior of the *c* parameter was reversible, the crystal was first cooled to R*T* in 50 K steps (downward empty triangles in Figure 2) and then heated to 623K, 923K, 948K, 973K, and 1023 K (upward empty triangles in Figure 2) and kept at this temperature for 160 h to allow for deprotonation, which was monitored at intervals of around 24h (empty diamonds in Figure 2). The reversal annealing of the deprotonated crystal was done at steps of 50 K down to R*T* (downward triangles in Figure 2). Measured unit-cell parameters are reported in Table 1 and plotted in Figure 2.

Data collections and structure refinements

Intensity data collections for structure refinements were made on crystal 3380B n. 7 at R*T*, 523 and 773 K during the first heating cycle and at R*T* at the end of the whole experiment described above. The R*T* data collection before the heating cycle was done with a Bruker AXS CCD

This is a preprint, the final version is subject to change, of the American Mineralogist (MSA)
Cite as Authors (Year) Title. American Mineralogist, in press.
DOI: https://doi.org/10.2138/am-2019-6966

diffractometer, ω-rotation frames (scan width 0.2°, scan time 10 s, sample-to detector distance 50 mm) were processed with the SAINT software (Bruker, 2003) and intensities were corrected for Lorentz and polarization effects; absorption effects were empirically evaluated by the SADABS software (Krause et al. 2015) and an absorption correction was applied to the data. Accurate unit-cell dimensions were calculated by least-squares refinement of the positions of 8179 independent reflections with $I > 10\ \sigma_I$ in the θ range 2-45°. For the H*T* data collections and the final R*T* data collection, all done with a Philips PW1100 diffractometer, a quadrant of intensity data was explored ($\pm h$, $+k$, $+l$). Raw intensities were corrected for Lorentz and polarization effects, and a semi-empirical absorption correction based on ψ scans (North et al. 1968) was applied. For all the datasets, unweighted structure refinements based upon *F* were made in space group *Pnma* starting from the atom coordinates of Cámara and Oberti (2005). A program written in Pavia was used, which allows the use of neutral versus ionized scattering curves for all the sites where solid solution does not occur, and of combinations of ionized scattering curves for all other sites (Cannillo et al. 1983). Scattering factors were taken from the International Tables for X-ray Crystallography (1999) and from Hovestreydt (1983) for O^{2-}. Based on our previous experience of refining amphibole structures, we chose to refine the occupancies of neutral vs. ionized scattering factors for the O and T sites (O vs. O^{2-} and Si vs. Si^{4+}), whereas fully ionized scattering factors for Li^{+}, Mg^{2+}, Fe^{2+} and Al^{3+} were assigned to the *M*1-4 sites and their relative occupancies were refined. This choice, that does not allow by itself for electroneutrality of the refined model, produces the best estimation of the mean atomic numbers for the *M*1-4 sites. The results of the structure refinements (SREF) are reported in Tables 2-6. The cif files, with F^2_O and $\sigma(F^2_O)$ included, have been deposited as supplementary material.

RESULTS

Unit-cell parameters and thermoelastic behavior

This is a preprint, the final version is subject to change, of the American Mineralogist (MSA)
Cite as Authors (Year) Title. American Mineralogist, in press.
DOI: https://doi.org/10.2138/am-2019-6966

Figure 2 shows the changes in the unit-cell parameters measured during the annealing cycle. The studied Fe-rich holmquistite has an unusual behavior both before and after deprotonation. During the first heating experiment, a clear non-linear behavior is observed for the *c* parameter. Notably, clear deviations from linear behavior in the thermal expansivity of monoclinic and orthorhombic amphiboles had been so far observed solely (after complete deprotonation) for the β angle of the Fe-rich kaersutite DL5 annealed to 1300 K (Oberti et al. 2011; manuscript in preparation) and was ascribed to cation exchange involving the *M*(4) site. A subsequent cooling to R*T* (open symbols in Figure 2) showed that the process causing non linearity is irreversible and is in agreement with the hypothesis of a complex cation exchange process to be discussed in a later section below.

Unit-cell dimensions measured during cooling of the partially deprotonated phase show a clear discontinuity at 820-800 K between two linear trends with different slopes for both the *b* and the *c* parameters (Figure 2). This discontinuity has never been noticed in other amphibole compositions. Unfortunately, we do not have structure refinements done before and after the discontinuities. However, because a phase transition with a change of space group can be discounted (we have evidence of the *Pnma* symmetry in all the data collections available), and cation ordering does not occur so rapidly under cooling, these discontinuities are to be related to the unusual crystal-chemistry of holmquistite, and they must reflect the occurrence of topological mismatch/re-arrangement, which will be also investigated in the next section. It is worth noting, however, that without this change in slope (i) the *c* parameter would have converged to the value of the starting composition and (ii) the slope of the *b* parameter observed for the partially deprotonated phase would have been much higher than that of the fully OH phase. Neither of these behaviors has been observed in monoclinic or orthorhombic amphiboles.

The evolution with temperature of unit-cell parameters of the studied Fe-rich holmquistite crystal were fitted either with a linear (*a* lattice parameter) or with a *T*-dependent second-order polynomial equation (*b* and *c* lattice parameters) to obtain axial thermal expansion coefficients.

Both equations were used for unit-cell volume expansion. For the partially deprotonated counterpart of Fe-rich holmquistite, linear fits were carried out in the full *T* range investigated for the *a* lattice parameter and limited to 773 K for *b*, *c* and *V* parameters as a discontinuity is observed at that temperature.

Least-squares fittings of the experimental data give the following results:

Fe-rich holmquistite (R*T*-923 K): $\alpha_a = 1.36(2)\times10^{-5}$; $\alpha_b = 0.55(1)\times10^{-5}$; $\alpha_c = 1.5(1)\times10^{-5} - 6.7(9)\times10^{-9}$; $\alpha_V = 3.5(3)\times10^{-5} - 0.8(3)\times10^{-8}$ (polynomial); $2.58(6)\times10^{-5}$ (linear).

Partially deprotonated Fe-rich holmquistite: $\alpha_a = 1.324(9)\times10^{-5}$ (R*T*-1023 K); $\alpha_b = 0.60(1)\times10^{-5}$ (R*T*-773 K); $\alpha_c = 0.68(2)\times10^{-5}$ (R*T*-773 K); $\alpha_V = 2.59(2)\times10^{-5}$ (R*T*-773 K).

Unit-cell parameters and deprotonation

Similar to the other orthorhombic or monoclinic amphiboles studied so far, a significant shortening in the unit-cell dimensions is observed as a consequence of the deprotonation process, which is locally balanced via oxidation of $^{C}Fe^{2+}$ (as suggested by the shortening of the *M*1,3-O3 and <*M*1,3-O> bond lengths in Table 4 and 5). However, as shown in the next section, oxidation in this sample occurs solely at the *M*1 site.

The amount of the oxo component ($^{W}O^{2-}$) in the annealed sample can be estimated based on the changes in the *M*1-*M*2 distance measured at R*T* before and after annealing (Table 5). Although the equations proposed in Figure 29 of Oberti et al. (2007) were calibrated on monoclinic calcium and sodium-calcium amphiboles, their slope is similar (0.054 and 0.051, respectively) in the two subgroups (as well as in sodium-amphiboles; Oberti, unpublished data) and hence can be confidently used also for the orthorhombic amphibole under investigation. The change observed for the two independent *M*1-*M*2 distances at R*T* before and after the heating cycle is 0.046 Å, which allows for an estimated deprotonation of ~0.85 *apfu* for the Fe-rich holmquistite 3380B n. 7. This value implies that the deprotonation process induced by 160 h at 1023 K does not involve all the available Fe, and that 0.57 residual Fe^{2+} *apfu* are present in the annealed crystal 3380B n. 7 (298R

This is a preprint, the final version is subject to change, of the American Mineralogist (MSA)
Cite as Authors (Year) Title. American Mineralogist, in press.
DOI: https://doi.org/10.2138/am-2019-6966

in Tables 2-6). This finding is consistent with a smaller shrinking in the unit-cell volume measured at 1023 K for crystal 3380B n. 7 (ΔV = 0.8%) with respect to that measured at 1073 K for the Fe-richer crystal 3380B n. 4 (with total site-scattering of C cations = 85.4) used as a preliminary test at the beginning of this work (ΔV = 1.14%).

Cation exchange and Fe oxidation at H*T*

Pioneering studied done *in situ* by powder neutron diffraction on cummingtonites had showed that temperature induces a significant exchange between B and C cations, and that the entrance of the larger cation in the *M*(1-3) sites can be detected within two hours. The $^{B}Fe^{2+}_{-1}\,^{C}Mg_{1}\,^{B}Mg_{1}\,^{C}Fe^{2+}_{1}$ exchange occurs in grunerite at $T > 673$ K (Reece et al. 2002), and the $^{B}Mn^{2+}_{-1}\,^{C}Mg_{1}\,^{B}Mg_{1}\,^{C}Mn^{2+}_{1}$ exchange occurs in mangano-cummingtonite at $T > 873$ K (Reece et al. 2000). This behavior is similar to what observed later in a $^{B}Fe^{2+}$-rich pargasite, where Fe^{2+} migration from the *M*(4) to the *M*(1-3) sites could be detected at 773 K (in sample Z2124, Oberti et al. 2011). For orthorhombic amphiboles, the H*T* study of anthophyllite showed a significant Mn^{2+}-Mg exchange, with Mn^{2+} migrating from the *M*4 to the *M*2 site at or beyond 670 K (Welch et al. 2011a). In gedrite, Fe^{2+} was shown to move from the *M*4 site to the *M*1,3 sites beyond 720 K, where it oxidizes to Fe^{3+} during deprotonation at 973 K (Zema et al. 2012). The present experiment was not designed to measure kinetics of cation exchange; we can only state that it can be detected (from the refined site-scattering values; Table 6) already at 523 K.

In Table 7, we report our best model of the site populations in crystal 3380B n. 7, which was obtained based on the results of the structure refinement. It is validated by the good agreement observed between the refined and calculated values of the site scattering and of the mean bond-lengths. The crystal-chemical composition of crystal 3380B n. 7 does not allow the $^{B}Fe^{2+}_{-1}\,^{C}Mg_{-1}\,^{B}Mg_{1}\,^{C}Fe^{2+}_{1}$ exchange observed in the other amphibole compositions. Because all Fe is required to be a C cation in order to fit the refined site-scattering values, the only crystal-chemically feasible

This is a preprint, the final version is subject to change, of the American Mineralogist (MSA)
Cite as Authors (Year) Title. American Mineralogist, in press.
DOI: https://doi.org/10.2138/am-2019-6966

exchange in this sample is the migration of Li^{+} from the *M*4 to the *M*3 site, which couples with that of the smaller Mg^{2+} ions towards the *M*4 site.

During annealing to 773 K, we observe a small but reliable decrease in the site-scattering values refined at the *M*3 site and an increase in those refined at the *M*4 site (Table 6). This observation might in principle be due to a lower quality of the data collected at H*T*, because the site-scattering values refined at the other sites only show small changes without clear trends, but the refined value of the total number of electrons (Σ(B+C) in Table 6) remains almost constant, thus validating SREF analysis. Also, this trend is confirmed by the R*T* refinement of the partially deprotonated crystal, where a lower site-scattering value refined at the *M*3 site couples to higher values refined at the other *M* sites. A tentative pattern of site populations occurring after the annealing cycle is also reported in Table 7, where the oxidation of Fe has been accepted only at the *M*1 site based on the changes in refined site-scattering values and mean bond lengths. These results correspond to a crystal-chemical formula $^{A}(K_{0.01}\,Na_{0.01})\ ^{B}(Li_{1.83}Mg_{0.15}Na_{0.02})\ ^{C}(Mg_{1.63}Fe^{2+}_{0.57}\ Fe^{3+}_{0.85}Mn^{2+}_{0.02}Al_{1.88}\ Li_{0.05})\ ^{T}Si_{8.00}\ O_{22}\ ^{W}[O_{0.85}(OH_{1.12})F_{0.03}]$. In conclusion, SREF results are consistent with 0.26 Fe *apfu* migrating from *M*3 to *M*1 (0.08 *apfu*, exchanged with Mg) and especially to *M*2 (0.18 *apfu*, exchanged with Al) and of 0.05 Mg *apfu* from *M*3 to *M*4 (exchanged with Li; Table 7). The cation exchange involving the *M*4 site (which is not reversible on cooling, at least under the experimental conditions) is not related to deprotonation and is responsible of the non-linearity observed for the *c* unit-cell edge in Figure 2. The redistribution of Fe among the *M*1, *M*2 and *M*3 sites is most probably related to deprotonation, because its markers, such as the changes in the refined site-scattering values and in the <*M*1-3-O> distances, are evident only in the refinement done at the end of the annealing cycle (298R: Tables 4 and 6, respectively). It is hard to say whether or not the increase of Fe at *M*2 is related to the discontinuities in the B and C trends observed ~820 K during reversal, although is difficult to think of a cation exchange occurring quickly and during cooling.

This is a preprint, the final version is subject to change, of the American Mineralogist (MSA)
Cite as Authors (Year) Title. American Mineralogist, in press.
DOI: https://doi.org/10.2138/am-2019-6966

299 The contraction of the <*M*1,3-O> distances found in sample 298R are therefore due both to
300 Fe^{2+} oxidation to Fe^{3+} and to this complex cation exchange. The amount of Fe^{3+} required to locally
301 balance deprotonation is ordered at *M*1, as suggested by the refined mean bond-lengths (Table 7),
302 and is coherent with the oxo component formerly evaluated based on the *M*1-*M*2 distance. The
303 mean-square relative deviation from the average (Δ) and quadratic elongation (λ) of the *M*1 and *M*3
304 octahedra also change significantly after deprotonation because of the stronger contraction of the
305 bonds involving the O3 oxygen atoms, especially *M*1-O3A (from 2.094 to 1.986 Å), and the
306 lengthening of the *M*1-O2A,B bonds (from 2.107 to 2.113 Å and from 2.117 to 2.128 Å,
307 respectively). Although the <*M*4-O> distance increases only slightly (2.335 vs. 2.337 Å), the
308 pattern of the individual bond distances changes significantly in the partially deprotonated crystal,
309 where *M*4-O2A, *M*4-O4A,B and *M*4-O5A lengthen whereas *M*4-O2B, and particularly *M*4-O5B
310 and *M*4-O6B shorten. To sum up, thermal annealing does affect significantly both cation
311 distribution and polyhedral geometry.
312
313 **Evolution with *T* of the coordination polyhedra**
314 Table 4 reports the evolution of the geometrical descriptors of the individual polyhedral in
315 the Fe-rich holmquistite crystal 3380B n. 7, and Table 5 reports the evolution of the individual
316 distances. Note that distances measured at H*T* have been corrected for riding motion (Busing 1964).
317 As expected, the thermal expansion recorded for the four independent tetrahedra is very low. It is
318 interesting to note, however, that the *T*1A tetrahedron in the partially deprotonated crystal is
319 significantly smaller (<*T*1-O> from 1.618 to 1.610 Å) although the *T*1A-O1 distance increases
320 slightly; also, its angular variance at the end of the annealing is less than half that in the crystal
321 before annealing, whereas the quadratic elongation is constant to 1.000. In *T*1B, the trend is similar
322 but less pronounced in terms of <*T*1B-O>.

323 The mean bond lengths of the *M*1 and *M*3 polyhedra expand almost linearly (Table 5 and
324 Figure 3). The trends are compared in Figure 3 to those available for the other orthorhombic
325 amphiboles.
326 Polyhedral thermal expansivities were calculated for the individual *M* sites based on the
327 three structure refinement available under the hypothesis of a linear behavior, and are compared to
328 those available for orthorhombic amphiboles in Table 8 and Figure 4. Polyhedra expand less in the
329 studied Fe-rich holmquistite than in anthophyllite (Welch et al. 2011a) and gedrite (Zema et al.
330 2012), confirming that this amphibole composition implies some strong structural constraints.
331 In contrast to gedrite and anthophyllite, the sizes of the *M*1 and *M*3 octahedra in Fe-rich
332 holmquistite are almost identical. Also, their shrinking after the deprotonation process is quite
333 similar. It is important to note, however, that this feature does not depend on the oxidation of
334 similar quantities of Fe in the two sites (actually, almost all Fe oxidation occurs at *M*1) but on the
335 coupling of significant cation exchange (the incorporation of Li^{+} at the *M*3 site) and of Al disorder
336 between the *M*2 and the *M*3 sites.
337 The *M*2 octahedron has quite an anomalous behavior. In the partially deprotonated crystal,
338 the refined site-scattering increases by ~2 electron per formula unit, and the octahedron becomes
339 larger (<*M*2-O> increases from 1.931 to 1.940 Å), both features being coherent with the increase in
340 Fe^{2+}. However, its shortest bonds, *M*2-O4A and especially *M*2-O4B, shorten (from 1.829 to 1.827 Å
341 and from 1.839 to 1.824 Å, respectively). As a consequence, all the descriptors of the distortions of
342 the octahedron increase significantly after deprotonation. This behavior can be explained by the
343 need for further bond-valence contribution to the O4 oxygen atoms (which coordinate also *M*4 and
344 *T*2A,B, respectively).
345 Focusing on the *M*4 site, Table 5 shows that the *M*4-O6B distance has an unusual behavior,
346 because it shortens during annealing at H*T*. This behavior can be detected already at 523 K.
347 However, after deprotonation, a further structural rearrangement takes place, and the *M*4 site
348 geometries change accordingly. For instance, the *M*4-O4A and *M*4-O6B in the partly deprotonated

This is a preprint, the final version is subject to change, of the American Mineralogist (MSA)
Cite as Authors (Year) Title. American Mineralogist, in press.
DOI: https://doi.org/10.2138/am-2019-6966

crystal (2.176 and 2.674 Å, respectively) are longer than in the crystal at 773 K (2.156 and 2.616 Å, respectively).

Evolution of the conformation of the double chains of tetrahedra

Figure 4 compares the evolution of the geometry of the double-chains of tetrahedra as a function of *T* and deprotonation in the three orthorhombic compositions of reference. The O5-O6-O5 angle is a measure the kinking along the *c* direction, whereas the *T*1-O7-*T*1-angle is a measure of the bowing along the *a* and *b* directions (red lines and purple arrow, respectively in Figure 1).

As a general comment, in the Fe-rich holmquistite of this work, the geometries of the two symmetry-independent double chains of tetrahedra (A: left; B: right) are more similar than in gedrite and anthophyllite. In holmquistite and anthophyllite (Si_8 in the unit formula) all the tetrahedra are occupied by Si, whereas in gedrite (Si_6Al_2 in the unit formula), half of the *T*1 tetrahedra are occupied by Al, which has a longer ionic radius than Si. Hence, the two independent Si_8 double-chains in anthophyllite and holmquistite are more stretched than the Si_6Al_2 double-chains in gedrite. Also, they are far less bowed in the studied Fe-rich holmquistite than in anthophyllite and gedrite. Therefore, the kinking and the bowing values measured for Fe-rich holmquistite both indicate a severe strain in the double-chains of tetrahedra.

Coherently, H*T* refinements show that the Si_8 double-chains of tetrahedra are far less expansible along *c* in Fe-rich holmquistite than in anthophyllite, which is also in tune with the presence of a much smaller and less expansible *M*2 site occupied by Al (similar to gedrite). It is also interesting to note the very different evolution of the bowing and kinking angles measured after the deprotonation process in Fe-rich holmquistite and in gedrite: the partially deprotonated Fe-rich holmquistite 3380B n. 7 shows almost no change in the kinking of the B double-chain and an increase in that of the A double-chain (whereas gedrite shows a decrease). The increase in the bowing with deprotonation is more significant in Fe-rich holmquistite (Δ bowing = 1.9 and 2,1°, respectively, for the A and B double-chains; H loss = 0.85 apfu) than in gedrite (Δ bowing = 1.9 and

This is a preprint, the final version is subject to change, of the American Mineralogist (MSA)
Cite as Authors (Year) Title. American Mineralogist, in press.
DOI: https://doi.org/10.2138/am-2019-6966

375 0.7°, respectively, for the A and B double-chains; H loss = 1.12 apfu), especially for the B double-
376 chain.

377 These observations may spread a new light on the discontinuities observed at 820 K in the *b*
378 and *c* parameters during cooling of the partially deprotonated Fe-rich holmquistite of this work,
379 where the double-chains of tetrahedra (especially A) at R*T* are more stretched and more bowed than
380 in the untreated crystal. The main factor affecting the *c* edge in amphiboles is the dimension and
381 conformation of the double-chain of tetrahedra, whereas that affecting the *b* edge is the size of the
382 strip of octahedra (Hawthorne & Oberti 2007). The double-chains of tetrahedra maintain their
383 composition but the strip of octahedra has smaller *M*1 and *M*3 sites but larger *M*2 sites in the
384 partially deprotonated phase. Hence, the different thermal expansivity of the two units may bring to
385 a structural mismatch, which is avoided by a change in conformation of the double-chains of
386 tetrahedra. This in turn implies a change in coordination of the *M*4 site, which indeed is the hinge
387 connecting the two main units of the amphibole structure. This mechanism is perfectly coherent
388 with the available SREF data.

389

390 **The peculiarity of holmquistite among orthorhombic amphiboles**

391 The Fe-rich holmquistite studied in this work has a unique H*T* behavior, concerning both
392 the non-linear trends observed during annealing at H*T* for the *c* edge and the unit-cell volume and,
393 most significantly, the discontinuity in the trends observed for the *b* and *c* parameters when cooling
394 the partially deprotonated phase. The non-linearity of the *c* parameters in Fe-rich holmquistite
395 disappears in the reversal experiment, and is related to the (irreversible) $^{M4}Li_{-1}{}^{M3}Mg_{-1}{}^{M4}Mg_{1}{}^{M3}Li_{1}$
396 exchange. The discontinuity in the α_b and α_c trends in the partially deprotonated phase derives both
397 from the cation exchanges involving the nature and distribution of ^{C}Fe (enrichment and oxidation of
398 Fe^{2+} at the *M*1 site and disorder of Al between the *M*2 and *M*3 sites) and some geometrical
399 constraint related to the matching of the double-chains of tetrahedra with the strip of octahedra. In

This is a preprint, the final version is subject to change, of the American Mineralogist (MSA)
Cite as Authors (Year) Title. American Mineralogist, in press.
DOI: https://doi.org/10.2138/am-2019-6966

400 particular, a comparison between the structures of the untreated and of the partially deprotonated
401 crystal suggests changes in the conformation of the double-chains of tetrahedra.
402 In order to confirm this conclusion, further H*T* structure refinements are required on the
403 partially deprotonated phase, but they should be done on a Fe-poor compositions which are
404 expected to be more stable.
405

406 **Constraints for the H*T* behavior of orthorhombic amphiboles**

407 The work done so far on the H*T* behavior of orthorhombic amphiboles allows fixing some
408 general rules:

409 1. The presence of two symmetry-independent double-chains of tetrahedra in space group
410 *Pnma* allows different conformations of the chains around the A and B cations and different
411 responses to thermal expansion and deprotonation. A cooperative effect of the A cations on
412 the deprotonation process was indeed observed in gedrite, which has preferential H loss at
413 O3A (Zema et al. 2012).
414 2. The loss of the protons implies significant changes (contraction) in unit-cell parameters
415 (hence in molar volume) as well as in site populations and polyhedral geometry. The
416 contraction in molar volume, however, is always smaller than thermal expansion.
417 3. The major factors affecting thermal behavior in orthorhombic amphiboles are the nature of
418 the B cations, the Fe^{2+} content and the balance of the effects of Al occurring as a C or T
419 cation. The greater stiffness of the holmquistite structure is determined by the dominance of
420 Li at the *M*4 site. Whereas ^{C}Al limits the expansion of the strip of octahedra, ^{T}Al provides
421 more flexibility to the double-chains of tetrahedra.
422 4. The critical factor allowing deprotonation is the availability of Fe^{2+}, both as a C or as a B
423 cation. $^{B}Fe^{2+}$ is involved in the process *via* a $Fe^{2+} \leftrightarrow Mg$ exchange between the *M*4 and the
424 *M*1,3 sites, which is particularly important in gedrite, where migration of $^{B}Fe^{2+}$ starts around

700 K. In the studied Fe-rich holmquistite, only a redistribution of Fe^{2+} among the *M*1-3 sites could be observed, while Fe oxidation occurs only at the *M*1 site. Also, in this case deprotonation does not proceed until consumption of Fe^{2+}. Actually, some Fe^{2+} migrates to the *M*2 site, where it is no longer available to maintain local electroneutrality at the O(3) oxygen atom.

IMPLICATIONS

Amphiboles are a widespread mineral phase in rocks of very different origin and composition. They are considered one of the most useful markers of rock evolution, because they are sensitive to changes in both composition and *T* and *P* condition of the system, and also because their cation ordering strongly depends on the *T* and *P* conditions of closure (reviewed by Oberti et al. 2007). Also, at high *T* amphibole may release significant amounts of H^+, which combines with O_2 at the crystal surface to produce H_2O. The first attempts to understand the mechanism and the dynamics of H^+ release and migration are reported in Della Ventura et al. (2018a,b). Also, the work done in Pavia on orthorhombic and monoclinic amphiboles (the published parts are cited in the introduction) shows that the onset *T* for deprotonation strongly depends on composition.

How, when and how much H_2O is released during geological processes is certainly an important issue for petrological studies and their related thermodynamic models, especially in subduction-related processes, where deprotonation and dehydration reactions are relevant because they affect rheological properties. Hence, developing a comprehensive crystal-chemical model of the H*T* behavior and of the deprotonation process in amphiboles based upon quantitative crystal-chemical knowledge is an important goal. However, this model must take into account all the relevant variables (composition, cation ordering, and perhaps also symmetry) and, thus, requires a large amount of experimental work on different compositions. This work provides the required data for compositions of pertinence to one of the fourth rootname of orthorhombic amphiboles,

450 holmquistite, but also allows prediction of the behavior of the other Li rich compositions of
451 monoclinic amphiboles.
452
453 **Acknowledgments:** Careful reviews by J.C. Chappell and an anonymous reviewer are warmly
454 acknowledged.
455

456 ## REFERENCES CITED

457

458 Bačik, P., Ozdín, D., Miglierini, M., Kardošová, P., Pentrák, M., and Haloda, J. (2011) Physics and
459 Chemistry of Minerals, 38, 599–611.
460 Bosi, F., Skogby, H., and Balić-Žunić, T. (2016a) Thermal stability of extended clusters in dravite:
461 a combined EMP, SREF and FTIR study. Physics and Chemistry of Minerals, 43, 395–407.
462 Bosi, F., Skogby, H., and Halenius, U. (2016b) Thermal induced cation redistribution in Fe-bearing
463 oxy-dravite and potential geothermometric implications. Contributions to Mineralogy and
464 Petrology, 171, 47–60.
465 Brown, I.D. and Shannon, R.D. (1973) Empirical bond strength-bond lengths curves for oxides.
466 Acta Crystallographica, A29, 266–282.
467 Bruker (2003) SAINT Software Reference Manual. Version 6. Bruker AXS Inc., Madison,
468 Wisconsin, USA.
469 Busing, W.R. and Levy, H.A. (1964) The effect of thermal motion on the estimation of bond
470 lengths from diffraction measurements. Acta Crystallographica, 17, 142–146.
471 Cámara, F. and Oberti, R. (2005) The crystal-chemistry of holmquistites: Ferroholmquistite from
472 Greenbushes (Western Australia) and hints for compositional constraints in ^{B}Li amphiboles.
473 American Mineralogist, 90, 1167–1176.

474 Cannillo, E., Germani, G., and Mazzi F. (1983) New crystallographic software for Philips PW11000
475 single crystal diffractometer. CNR Centro di Studio per la Cristallografia, Internal Report 2.
476 Della Ventura, G., Susta, U., Bellatreccia, F., Cavallo, A., and Oberti, R. (2015) Synthetic potassic-
477 ferro-richterite: *HT* behavior and deprotonation process by single-crystal FTIR spectroscopy
478 and structure refinement (abs). Rendiconti online Società Geologica Italiana, 35(2), 232.
479 Della Ventura, G., Mihailova, B., Susta, U., Cestelli Guidi, M., Marcelli, A., Schlüter, J., and
480 Oberti, R. (2018a) The dynamics of Fe oxidation in riebeckite: a model for amphiboles.
481 American Mineralogist, 103, 1103–1111.
482 Della Ventura, G., Galdenzi, F., Cibin, G., Oberti, R., Xu, W., Macis, S., and Marcelli, A. (2018b)
483 Iron oxidation dynamics vs. temperature of synthetic potassic-ferro-richterite: a XANES
484 investigation. Physical Chemistry Chemical Physics, 20, 21764-21771.
485 Filip, J., Bosi, F., Novak, M., Skogby, H., Tuček, J., Čuda, J., and Wildner, M. (2012) Iron redox
486 reactions in the tourmaline structure: high-temperature treatment of Fe^{3+}-rich schorl.
487 Geochimica et Cosmochimica Acta, 86, 239–256.
488 Frost, M.T., Tsambourakis, G., and Davis J. (1987) Holmquistite-bearing amphibolite from
489 Greenbushes, Western Australia. Mineralogical Magazine, 51, 585–591.
490 Fuchs, Y., Lagache, M., and Linares, J. (2002) Oxydation expérimentale de Fe-tourmalines et
491 corrélation avec une déprotonation des groupes hydroxyle. C. R. Geoscience, 334, 245-249.
492 Gualtieri, AF, Giacobbe, C, and Viti C (2012) The dehydroxylation of serpentine group minerals.
493 American Mineralogist, 97, 666–680.
494 Hawthorne, F.C. and Oberti, R. (2007) Amphiboles: Crystal-chemistry. Rev Mineral Geochem 67:1-
495 54
496 Hawthorne, F.C., Oberti, R., Harlow, G.E., Maresch, W.V., Martin, R.F., Schumacher, J.C., and
497 Welch, M.D. (2012) Nomenclature of the amphibole supergroup. American Mineralogist, 97,
498 2031–2048.

499 Hovestreydt, E. (1983) On the atomic scattering factor for O^{2-}. Acta Crystallographica, A39,
500 268–269.
501 International Tables for X-ray Crystallography (1999) Volume C*:* Mathematical, physical and
502 chemical tables. International Union of Crystallography, 2nd Edition, eds AJC Wilson and E
503 Prince
504 Krause, L., Herbst-Irmer, R., Sheldrick, G.M,. and Stalke, D. (2015) Comparison of silver and
505 molybdenum microfocus X-ray sources for single-crystal structure determination. Journal of
506 Applied Crystallography, 48, 3–10.
507 North, A.C.T., Phillips, D.C., and Mathews, F.S. (1968) A semi-empirical method of absorption
508 correction. Acta Crystallographica, A24, 351–359.
509 Nestola, F., Pasqual, D., Welch, M.D., and Oberti, R. (2012) The effects of composition upon the
510 high-pressure behaviour of amphiboles: compression of gedrite to 7 GPa and a comparison with
511 anthophyllite and proto-amphibole. Mineralogical Magazine, 76, 987–995.
512 Oberti, R., Hawthorne, F.C., Cannillo, E., and Cámara, F. (2007) Long-range order in amphiboles. In:
513 Amphiboles: Crystal Chemistry, Occurrence and Health Issues (F.C. Hawthorne, R. Oberti, G.
514 Della Ventura and A. Mottana eds.). Reviews in Mineralogy and Geochemistry, 67, 125–172.
515 Oberti, R., Zema, M., Tarantino, S., and Boiocchi, M. (2009) HT behaviour of pargasite and
516 kaersutite: expansivity coefficients and dehydrogenation mechanisms (abs). 38° meeting of the
517 Italian Crystallographic Association, Atti, 98.
518 Oberti, R., Zema, M., Boiocchi, M., Tarantino, S.C., and Welch, M.D. (2011) HT-induced
519 processes in monoclinic and orthorhombic amphiboles and their effects on thermodynamic
520 models (abs). Geophysical Researches Abs, 13, EGU2011, 11183.
521 Oberti, R., Boiocchi, M., Zema, M., and Della Ventura, G. (2016) Synthetic potassic-ferro-
522 richterite: 1. Composition, crystal structure refinement and H*T* behavior by *in operando* single-
523 crystal X-ray diffraction. Canadian Mineralogist, 54, 353–369.

524 Oberti, R., Boiocchi, M., Zema, M., Hawthorne, F.C., Redhammer, G., Susta, U., and Della
525 Ventura, G. (2018) The H*T* behavior of riebeckite: Expansivity, deprotonation, selective Fe
526 oxidation and a novel cation disordering scheme for amphiboles. European Journal of
527 Mineralogy, in press. DOI: 10.2138/am-2018-6382.
528 Partington, G.A., McNaughton, N.J., and Williams, I.S. (1995) A review of the geology,
529 mineralisation and geochronology of the Greenbushes Pegmatite, Western Australia. Economic
530 Geology, 90, 616–635.
531 Pieczka, A. and Kraczka, J. (2004) Oxidized tourmalines – a combined chemical, XRD and
532 Mössbauer study. European Journal of Mineralogy, 16, 309–321.
533 Reece, J.J., Redfern, S.A.T., Welch, M.D., and Henderson, C.M.B. (2000) Mn-Mg disordering in
534 cummingtonite: a high-temperature neutron powder diffraction study. Mineralogical Magazine,
535 64, 255–266.
536 Reece, J.J., Redfern, S.A.T., Welch, M.D., Henderson, C.M.B., and McCammon, C.A. (2002)
537 Temperature-dependent Fe^{2+}–Mn^{2+} order–disorder behaviour in amphiboles. Physics and
538 Chemistry of Minerals 29, 562–570.
539 Robinson, K., Gibbs, G.V., and Ribbe, P.H. (1971) Quadratic elongation: a quantitative measure of
540 distortion in coordination polyhedra. Science, 172, 567–570.
541 Sueno, S., Matsuura, S., Bunno, M., and Kurosawa, M. (2002) Occurrence and crystal-chemical
542 features of protoferro-anthophyllite and protomangano-ferro-anthophyllite from Cheyenne
543 Canyon and Cheyenne Mountain, USA, and Hirukawa-mura, Suisho-yama, and Yokone-yama,
544 Japan. Japan Mineralogy and Petrology Sciences, 97, 127–136.
545 Trittschack, R. and Grobéty, B. (2012) Dehydroxylation kinetics of lizardite. European Journal of
546 Mineralogy, 24, 47–57.
547 Trittschack, R. and Grobéty, B. (2013) The dehydroxylation of chrysotile: A combined in situ
548 micro-Raman and micro-FTIR study. American Mineralogist, 98, 1133–1145.

549 Ventruti, G., Zema, M., Scordari, F., and Pedrazzi, G. (2008) Thermal behaviour of a Ti-rich
550 phlogopite from Mt. Vulture (Potenza, Italy): an in situ X-ray single crystal diffraction study.
551 American Mineralogist, 93, 632–643.
552 Welch, M.D., Cámara, F., Della Ventura, G., and Iezzi, G. (2007) Non-ambient in situ studies of
553 amphiboles. In Amphiboles: Crystal Chemistry, Occurrence, and Health Issues (F.C.
554 Hawthorne, R. Oberti, G. Della Ventura, & A. Mottana, eds.) Reviews in Mineralogy and
555 Geochemistry, 67, 223–260.
556 Welch, M.D., Cámara, F., and Oberti, R. (2011a) Thermoelasticity and high-*T* behaviour of
557 anthophyllite. Physics and Chemistry of Minerals, 38, 321–334.
558 Welch, M.D., Gatta, G.D., and Rotiroti, N. (2011b) The high-pressure behavior of orthorhombic
559 amphiboles. American Mineralogist, 96, 623–630.
560 Yang, X., Keppler, H., and Li, Y. (2016) Molecular hydrogen in mantle minerals. Geochemical
561 Perspectives Letters, 2, 160–168.
562 Zanazzi, P.F., Nestola, F., and Pasqual, D. (2010) Compressibility of protoamphibole: a high-
563 pressure single-crystal diffraction study of protomanganoferro-anthophyllite. American
564 Mineralogist, 95, 1758–1764.
565 Zema, M., Ventruti, G., Lacalamita, M., and Scordari, F. (2010) Kinetics of Fe-
566 oxydation/deprotonation process in Fe-rich phlogopite under isothermal conditions. American
567 Mineralogist, 95, 1458–1466.
568 Zema, M., Welch, M.D., and Oberti, R. (2012) High-*T* behaviour of gedrite: thermoelasticity and
569 dehydrogenation. Contributions to Mineralogy and Petrology, 163, 923–937.

This is a preprint, the final version is subject to change, of the American Mineralogist (MSA)
Cite as Authors (Year) Title. American Mineralogist, in press.
DOI: https://doi.org/10.2138/am-2019-6966

570

571 **List of figure captions**

572

573 **FIGURE 1.** The crystal structure of Fe-rich holmquistite 3380B n.7 at R*T* projected onto (100). The
574 relevant site nomenclature is shown according to Hawthorne and Oberti (2007). The red line
575 indicates the kinking angle (O5-O6-O5), and the purple arrow the bowing angle (*T*1-O7-*T*1)
576 for the B double-chain of tetrahedra.

577 **FIGURE 2.** Changes in unit-cell parameters measured for Fe-rich holmquistite 3380B n. 7 during
578 thermal annealing. All events recorded are reported in the graph: first heating to 923K
579 (upward solid triangles); cooling to R*T* (downward empty triangles); re-heating up to 1023K
580 (empty upward triangles); isothermal annealing at 1023K for 160 h (empty diamonds)
581 showing contraction of all parameters due to the occurring of the deprotonation process; final
582 cooling to R*T* of the deprotonated crystal (downward solid triangles).

583 **FIGURE 3.** Changes in mean bond-lengths (corrected by riding motion) at the *M*1-3 octahedra and at
584 the *M*4 [6+2] coordinated site observed during annealing in anthophyllite (left), gedrite
585 (middle) and Fe-rich holmquistite 3380 n. 7 (right). Solid symbols: the original crystal; empty
586 symbols: the deprotonated crystal.

587 **FIGURE 4.** The evolution of the volumes of the individual polyhedra in holmquistite and in the other
588 orthorhombic amphiboles studied so far. The calculated thermal expansivities are reported
589 and compared in Table 8.

590 **FIGURE 5.** Changes in the kinking (O5-O6-O5) and bowing (*T*1-O7-*T*1) angles in the two
591 independent double chains of tetrahedra (A and B) measured in orthorhombic amphiboles
592 during thermal annealing. Solid symbols: the original crystal; empty symbols: the
593 deprotonated crystal.

This is a preprint, the final version is subject to change, of the American Mineralogist (MSA)
Cite as Authors (Year) Title. American Mineralogist, in press.
DOI: https://doi.org/10.2138/am-2019-6966

Table 1 Changes in unit-cell parameters of Fe-rich holmquistite 3380B n. 7 as a function of *T*.

T (K)	*a* (Å)	*b* (Å)	*c* (Å)	*V* (Å^3)
Heating				
298	18.2622(11)	17.6481(10)	5.2716(3)	1699.00(3)
323	18.2609(13)	17.6447(12)	5.2709(4)	1698.33(4)
373	18.2729(9)	17.6498(8)	5.2736(3)	1700.80(2)
423	18.2864(8)	17.6577(8)	5.2760(3)	1703.60(2)
473	18.2975(9)	17.6609(9)	5.2789(3)	1705.88(2)
523	18.3146(11)	17.6661(8)	5.2809(3)	1708.62(3)
573	18.3268(11)	17.6733(8)	5.2831(3)	1711.17(3)
623	18.3392(12)	17.6764(10)	5.2859(4)	1713.54(4)
673	18.3501(12)	17.6826(9)	5.2860(3)	1715.19(3)
723	18.3674(10)	17.6858(7)	5.2879(3)	1717.73(2)
773	18.3768(11)	17.6924(8)	5.2894(3)	1719.74(3)
823	18.3869(10)	17.6947(8)	5.2899(3)	1721.07(2)
873	18.4007(7)	17.6995(6)	5.2913(3)	1723.29(2)
923	18.4098(10)	17.7043(8)	5.2913(4)	1724.61(3)
Reversal 1				
848	18.3864(11)	17.6949(9)	5.2886(4)	1720.62(4)
798	18.3736(9)	17.6910(8)	5.2876(3)	1718.72(2)
748	18.3566(10)	17.6855(7)	5.2860(3)	1716.08(2)
698	18.3481(9)	17.6821(7)	5.2840(3)	1714.30(2)
648	18.3339(9)	17.6755(7)	5.2830(3)	1712.01(2)
598	18.3213(10)	17.6698(8)	5.2816(3)	1709.83(2)
548	18.3078(10)	17.6646(9)	5.2789(3)	1707.20(3)
498	18.2964(10)	17.6604(9)	5.2771(4)	1705.15(3)
448	18.2815(8)	17.6544(6)	5.2760(3)	1702.82(2)
398	18.2700(10)	17.6484(9)	5.2737(3)	1700.43(3)
348	18.2577(11)	17.6440(11)	5.2713(4)	1698.09(4)
623	18.3266(10)	17.6728(9)	5.2823(3)	1710.84(3)
923	18.4069(13)	17.7010(9)	5.2900(4)	1723.59(4)
948	18.4101(11)	17.7070(9)	5.2918(4)	1725.06(4)
973	18.4186(13)	17.7078(9)	5.2904(4)	1725.48(4)
1023	18.4278(14)	17.7136(11)	5.2918(5)	1727.36(6)
1023	18.4110(15)	17.7018(12)	5.2854(5)	1722.55(6)
1023	18.4041(10)	17.6988(9)	5.2865(3)	1721.97(3)
1023	18.3964(11)	17.6929(8)	5.2823(3)	1719.31(3)
1023	18.3879(9)	17.6881(7)	5.2789(3)	1716.95(2)
1023	18.3834(10)	17.6818(7)	5.2777(3)	1715.52(2)
1023	18.3750(9)	17.6738(7)	5.2740(3)	1712.76(2)
Reversal 2: partially deprotonated				
*1023	18.3750(10)	17.6818(7)	5.2740(3)	1713.54(2)
973	18.3625(9)	17.6663(7)	5.2739(3)	1710.84(2)
923	18.3493(9)	17.6566(6)	5.2724(3)	1708.19(2)
873	18.3380(11)	17.6494(9)	5.2715(3)	1706.15(3)
823	18.3227(9)	17.6443(9)	5.2712(4)	1704.13(3)

773	18.3144(11)	17.6250(9)	5.2683(4)	1700.56(3)
723	18.3019(12)	17.6174(9)	5.2672(4)	1698.31(4)
673	18.2907(13)	17.6137(10)	5.2648(4)	1696.14(4)
623	18.2753(11)	17.6061(9)	5.2641(4)	1693.76(3)
573	18.2648(12)	17.6013(10)	5.2620(4)	1691.65(4)
523	18.2516(10)	17.5939(7)	5.2602(3)	1689.14(2)
473	18.2398(10)	17.5909(8)	5.2581(3)	1687.09(2)
423	18.2281(10)	17.5860(8)	5.2566(4)	1685.05(3)
373	18.2194(11)	17.5810(9)	5.2539(4)	1682.90(3)
323	18.2039(12)	17.5751(10)	5.2521(3)	1680.33(3)
298	18.2000(6)	17.5742(6)	5.2523(3)	1679.95(2)

* Measured after 160 hr of further isothermal annealing at 1023 K

Table 2 Unit-cell parameters and relevant information for data collection and structure refinements for Fe-rich holmquistite 3380B n. 7 measured at different *T* values.

	Fe-rich holmquistite			partially deprotonated
T (K)	298*	523	773	298**
a (Å)	18.2730(5)	18.3128(11)	18.3739(11)	18.2000(6)
b (Å)	17.6553(5)	17.6649(9)	17.6890(8)	17.5742(6)
c (Å)	5.27400(10)	5.2816(3)	5.2890(3)	5.2523(3)
V (Å^3)	1701.47(7)	1708.6(2)	1719.0(2)	1679.95(12)
θ range (°)	2-45	2-27	2-27	2-27
Reflections unique	7199	1839	1850	1802
R_{int} (%)	1.9	2.6	3.1	3.0
Reflections $I > 3\sigma_I$	5835	1173	1155	1146
R_1 (obs) %	2.6	2.4	2.7	3.4
R_{all} %	3.3	5.3	6.1	6.5

* CCD data; ** Collected at the end of the reversal experiment

This is a preprint, the final version is subject to change, of the American Mineralogist (MSA)
Cite as Authors (Year) Title. American Mineralogist, in press.
DOI: https://doi.org/10.2138/am-2019-6966

Table 3 (deposited)

Atom coordinates and atom displacement parameters (B_{eq}, Å²; β x 10^4) for Fe-rich holmquistite 3380B n. 7 and its partially deprotonated counterpart.

site	*x/a*	*y/b*	*z/c*	B_{eq}	β_{11}	β_{22}	β_{33}	β_{12}	β_{13}	β_{23}
298 K										
O1A	0.18064(3)	0.15629(4)	0.04977(12)	0.610(8)	4	5	63	0	0	1
O1B	0.06982(3)	0.15590(4)	0.73957(12)	0.620(8)	4	5	61	0	1	0
O2A	0.18438(3)	0.07523(4)	0.59277(12)	0.641(8)	4	6	63	0	0	0
O2B	0.06511(3)	0.07469(4)	0.19877(12)	0.648(8)	4	6	63	0	1	1
O3A	0.18222(5)	1/4	0.55444(19)	0.76(2)	5	7	72	-	1	-
O3B	0.06849(5)	1/4	0.23515(19)	0.75(2)	5	6	74	-	1	-
O4A	0.31271(4)	-0.00409(4)	0.56265(13)	0.779(9)	6	5	77	2	2	-1
O4B	-0.06488(4)	-0.00130(4)	0.26767(13)	0.773(9)	6	6	70	-2	-1	3
O5A	0.30541(4)	0.11492(4)	-0.16381(13)	0.774(11)	5	8	57	0	0	-8
O5B	-0.05439(4)	0.11369(4)	0.95068(13)	0.781(8)	5	8	61	0	0	8
O6A	0.29671(4)	0.12971(4)	0.33666(13)	0.856(11)	6	9	59	-1	-3	8
O6B	-0.04650(4)	0.13300(4)	0.45010(13)	0.869(11)	6	9	59	1	-2	-10
O7A	0.29334(6)	1/4	0.04452(21)	0.88(2)	7	4	111	-	2	-
O7B	-0.04269(6)	1/4	0.75600(21)	0.89(2)	7	4	108	-	0	-
*T*1A	0.26953(2)	0.16201(2)	0.06783(5)	0.487(6)	4	4	44	0	0	0
*T*1B	-0.01901(2)	0.16239(2)	0.72351(5)	0.491(7)	4	4	44	0	0	0
*T*2A	0.27346(2)	0.07606(2)	0.57408(5)	0.498(6)	4	4	44	1	0	0
*T*2B	-0.02408(2)	0.07697(2)	0.21531(5)	0.512(7)	4	4	44	-1	1	0
*M*1	0.12521(2)	0.15883(2)	0.39480(4)	0.612(6)	5	5	46	0	1	0
*M*2	0.12541(2)	0.06858(2)	-0.10390(5)	0.533(7)	4	4	49	0	0	1
*M*3	0.12532(2)	1/4	-0.10559(5)	0.583(7)	5	4	52	-	-1	-
*M*4	0.12372(12)	-0.00925(12)	0.39795(38)	1.46(4)	11	15	95	2	7	4
H1	0.2261(14)	1/4	0.5545(48)	1.0						
H2	0.0274(14)	1/4	0.2309(49)	1.0						
523 K										
O1A	0.1805(2)	0.1558(2)	0.0507(5)	0.76(7)	6	6	70	0	-1	1
O1B	0.0700(2)	0.1560(2)	0.7417(6)	0.90(7)	5	9	79	0	3	1
O2A	0.1844(2)	0.0749(2)	0.5972(6)	0.81(7)	4	8	79	1	-2	0
O2B	0.0648(2)	0.0748(2)	0.2001(6)	0.82(7)	4	8	77	0	-1	-1
O3A	0.1822(3)	1/4	0.5560(8)	1.06(11)	6	8	118	-	3	-
O3B	0.0690(2)	1/4	0.2367(8)	1.21(12)	8	12	95	-	1	-
O4A	0.3128(2)	-0.0037(2)	0.5648(6)	1.13(8)	9	9	94	3	4	2
O4B	-0.0645(2)	-0.0015(2)	0.2628(6)	0.96(7)	8	7	90	-2	-5	3
O5A	0.3052(2)	0.1160(2)	-0.1649(6)	1.10(8)	5	15	72	1	0	-10
O5B	-0.0538(2)	0.1151(2)	0.9555(6)	1.14(8)	6	15	67	0	-1	13
O6A	0.2960(2)	0.1292(2)	0.3364(6)	1.22(8)	8	15	75	-1	-5	12
O6B	-0.0463(2)	0.1311(2)	0.4563(6)	1.36(8)	5	20	87	1	-1	-19
O7A	0.2926(3)	1/4	0.0489(9)	1.20(11)	10	6	139	-	3	-
O7B	-0.0421(3)	1/4	0.7496(9)	1.13(11)	7	6	161	-	-1	-
*T*1A	0.26904(7)	0.16208(7)	0.0689(2)	0.62(3)	4	6	47	0	1	1
*T*1B	-0.01871(7)	0.16233(7)	0.7256(2)	0.65(3)	4	7	48	0	0	0
*T*2A	0.27336(7)	0.07626(7)	0.5752(2)	0.61(3)	4	6	47	1	0	0
*T*2B	-0.02398(7)	0.07708(7)	0.2164(2)	0.64(3)	4	7	46	-1	1	-1
*M*1	0.12521(6)	0.15871(5)	0.3968(2)	0.79(2)	7	8	46	0	1	-1
*M*2	0.12553(7)	0.06818(6)	-0.1013(2)	0.66(3)	5	7	48	0	1	0
*M*3	0.12523(8)	1/4	-0.1038(3)	0.78(3)	7	7	57	-	-2	-
*M*4	0.1225(6)	-0.0089(4)	0.400(2)	2.2(2)	19	19	155	1	16	6
H1	0.224(4)	1/4	0.537(12)	1.0						

H2	0.0287(4)	1/4	0.2488(12)	1.0						
773 K										
O1A	0.1805(2)	0.1558(2)	0.0518(6)	1.11(9)	7	9	104	1	2	3
O1B	0.0700(2)	0.1558(2)	0.7421(6)	1.05(9)	6	12	81	-1	4	0
O2A	0.1847(2)	0.0746(2)	0.5976(7)	1.12(8)	4	14	91	2	3	2
O2B	0.0647(2)	0.0746(2)	0.2011(7)	1.10(8)	7	12	84	0	2	0
O3A	0.1821(3)	1/4	0.5569(10)	1.46(14)	5	14	175	-	7	-
O3B	0.0691(3)	1/4	0.2380(10)	1.6(2)	11	16	116	-	4	-
O4A	0.3130(2)	-0.0032(2)	0.5662(7)	1.44(9)	11	12	122	4	2	-1
O4B	-0.0642(2)	-0.0012(2)	0.2601(7)	1.44(9)	11	12	132	-5	-3	1
O5A	0.3044(2)	0.1170(2)	-0.1647(7)	1.34(9)	7	16	98	0	2	-15
O5B	-0.0536(2)	0.1168(2)	0.9584(7)	1.42(9)	8	15	109	-1	1	20
O6A	0.2955(2)	0.1285(2)	0.3352(7)	1.49(10)	9	16	109	0	-6	16
O6B	-0.0463(2)	0.1292(2)	0.4596(7)	1.77(10)	10	23	106	2	-5	-26
O7A	0.2917(3)	1/4	0.0539(11)	1.8(2)	9	12	220	-	-2	-
O7B	-0.0416(3)	1/4	0.7465(11)	1.70(14)	14	8	208	-	-1	-
*T*1A	0.26874(8)	0.16226(8)	0.0698(3)	0.79(3)	6	8	57	0	0	0
*T*1B	-0.01848(8)	0.16242(8)	0.7267(3)	0.79(3)	5	7	70	-1	0	-1
*T*2A	0.27314(8)	0.07644(8)	0.5764(3)	0.81(3)	6	8	63	2	0	1
*T*2B	-0.02381(8)	0.07716(8)	0.2175(3)	0.84(3)	5	9	60	-1	1	-2
*M*1	0.12525(7)	0.15861(6)	0.3984(2)	1.21(3)	10	11	80	0	1	0
*M*2	0.12565(8)	0.06761(7)	-0.0994(3)	0.98(3)	7	9	81	0	0	0
*M*3	0.12514(10)	1/4	-0.1022(3)	1.11(3)	10	8	95	-	-1	-
*M*4	0.1227(7)	-0.0124(5)	0.399(2)	3.4(3)	25	34	222	3	27	6
H1	0.221(4)	1/4	0.550(14)	1.0						
H2	0.036(4)	1/4	0.225(14)	1.0						
298 KR*										
O1A	0.1813(2)	0.1585(2)	0.0508(7)	0.71(10)	5	7	52	-1	0	3
O1B	0.0695(2)	0.1578(2)	0.7346(7)	0.61(10)	3	7	50	-1	6	0
O2A	0.1837(2)	0.0787(2)	0.5855(7)	0.57(9)	1	9	51	0	4	-5
O2B	0.0662(2)	0.0779(2)	0.2009(7)	0.62(9)	4	6	46	-1	-1	5
O3A	0.1799(4)	1/4	0.5559(11)	0.80(14)	8	3	88	-	-1	-
O3B	0.0705(4)	1/4	0.2278(11)	1.0(2)	7	6	128	-	-3	-
O4A	0.3104(2)	-0.0055(2)	0.5572(7)	0.69(10)	4	7	55	2	4	-3
O4B	-0.0632(3)	-0.0025(2)	0.2642(7)	0.76(10)	7	6	59	-1	-4	6
O5A	0.3051(2)	0.1147(2)	-0.1679(7)	0.61(9)	1	8	66	-1	-2	-5
O5B	-0.0543(2)	0.1132(2)	0.9501(7)	0.68(9)	5	7	49	-3	-1	10
O6A	0.2983(2)	0.1293(2)	0.3297(8)	0.76(10)	6	8	54	-1	-2	4
O6B	-0.0483(2)	0.1325(2)	0.4507(8)	0.88(10)	4	10	73	1	-6	-8
O7A	0.2962(3)	1/4	0.0413(11)	0.71(14)	5	4	89	-	-3	-
O7B	-0.0455(3)	1/4	0.7576(11)	0.75(14)	5	6	75	-	-2	-
*T*1A	0.27096(9)	0.16265(9)	0.0639(3)	0.40(4)	3	4	29	0	-2	0
*T*1B	-0.02043(9)	0.16305(9)	0.7228(3)	0.43(4)	3	4	38	0	1	2
*T*2A	0.27326(9)	0.07639(8)	0.5686(3)	0.41(3)	3	4	32	0	0	0
*T*2B	-0.02385(9)	0.07749(8)	0.2161(3)	0.40(3)	3	4	31	-1	0	0
*M*1	0.12522(8)	0.16513(6)	0.3932(3)	0.67(3)	4	9	37	0	1	-1
*M*2	0.12536(9)	0.06871(7)	-0.1059(3)	0.48(3)	3	5	41	0	1	0
*M*3	0.12545(13)	1/4	-0.1072(4)	0.47(5)	4	3	41	-	-3	-
*M*4	0.1217(5)	-0.0090(5)	0.395(2)	1.6(2)	12	21	57	3	12	5

* Collected at the end of the reversal experiment

Table 4 Geometrical parameters for all coordination polyhedra in Fe-rich holmquistite 3380B n. 7 and its partially deprotonated counterpart. $\square^2$ = Bond-Angle Variance, <□> = Quadratic Elongation (Robinson et al. 1971), Δ = mean-square relative deviation from the average for octahedra (Brown and Shannon, 1973). Mean bond-lengths at H*T* are corrected for riding motion (Busing and Levy 1964).

	*T*1A	*T*1B	*T*2A	*T*2B	*M*1	*M*2	*M*3	*M*4
298 K								
<*T*-O>, <*M*-O>.(Å)	1.618	1.617	1.624	1.625	2.096	1.931	2.097	2.335
V (Å^3)	2.17	2.17	2.18	2.19	11.90	9.47	11.79	17.04
$\square^2$ ($^{\circ 2}$)	0.68	1.20	17.95	15.29	68.43	30.53	90.25	
Δ					0.36	15.63	0.59	
<□>	1.000	1.000	1.005	1.004	1.021	1.010	1.028	
523 K								
<*T*-O>, <*M*-O>.(Å)	1.622	1.620	1.629	1.627	2.101	1.932	2.100	2.353
V (Å^3)	2.17	2.16	2.18	2.18	11.97	9.46	11.82	17.28
$\square^2$($^{\circ 2}$)	0.89	1.06	17.10	15.04	70.55	30.74	92.47	
Δ					0.42	16.06	0.54	
<□>	1.000	1.000	1.004	1.004	1.021	1.010	1.029	
773 K								
<*T*-O>, <*M*-O>.(Å)	1.621	1.623	1.629	1.627	2.106	1.939	2.105	2.359
V (Å^3)	2.16	2.16	2.18	2.17	12.05	9.55	11.90	17.50
$\square^2$($^{\circ 2}$)	0.84	0.61	15.67	15.30	69.19	31.37	92.39	
Δ					0.61	17.44	0.59	
<□>	1.000	1.000	1.004	1.004	1.021	1.011	1.029	
298 KR*								
<*T*-O>, <*M*-O>.(Å)	1.610	1.615	1.623	1.624	2.060	1.940	2.063	2.337
V (Å^3)	2.14	2.16	2.18	2.18	11.30	9.57	11.29	17.05
$\square^2$($^{\circ 2}$)	0.30	0.57	17.65	15.99	66.91	40.26	77.34	
Δ					6.89	22.07	1.65	
<□>	1.000	1.000	1.004	1.004	1.021	1.014	1.024	

* Collected at the end of the reversal experiment

$\Delta = \Sigma[((M\text{-O})_{i=1,6}\text{-}\langle M\text{-O}\rangle)/\langle M\text{-O}\rangle]^2/6\cdot 10^4$

Table 5. Evolution of the individual cation-oxygen distances in the different polyhedral, of kinking (O5-O6-O5) and bowing (*T*1-O7-*T*1) angles in the two independent double chains of tetrahedral, and of the *M*1-*M*2 interatomic distances during the annealing cycle. *T*-O and *M*-O bond-lengths at H*T* are corrected for riding motion (Busing and Levy 1964).

	298 K	523 K	773 K	298 KR*
*T*1A-O1A	1.6303(7)	1.629	1.632	1.634(5)
*T*1A-O5A	1.6167(7)	1.625	1.621	1.606(4)
*T*1A-O6A	1.6069(7)	1.612	1.611	1.594(4)
*T*1A-O7A	1.6179(4)	1.622	1.620	1.607(2)
*T*1B-O1B	1.6295(7)	1.633	1.635	1.640(5)
*T*1B-O5B	1.6102(7)	1.613	1.610	1.604(4)
*T*1B-O6B	1.6127(7)	1.615	1.625	1.609(4)
*T*1B-O7B	1.6152(4)	1.618	1.620	1.605(2)
*T*2A-O2A	1.6308(7)	1.636	1.633	1.633(4)
*T*2A-O4A	1.5877(7)	1.594	1.595	1.590(4)
*T*2A-O5A	1.6499(7)	1.654	1.655	1.644(4)
*T*2A-O6A	1.6265(7)	1.631	1.633	1.627(4)
*T*2B-O2B	1.6325(7)	1.631	1.632	1.641(5)
*T*2B-O4B	1.5943(7)	1.597	1.596	1.597(4)
*T*2B-O5B	1.6356(7)	1.634	1.640	1.629(4)
*T*2B-O6B	1.6370(7)	1.646	1.641	1.627(4)
*M*1-O1A	2.0830(7)	2.091	2.097	2.071(4)
*M*1-O1B	2.0817(7)	2.084	2.083	2.064(4)
*M*1-O2A	2.1066(7)	2.118	2.125	2.113(4)
*M*1-O2B	2.1170(7)	2.121	2.130	2.128(4)
*M*1-O3A	2.0940(7)	2.099	2.101	1.986(4)
*M*1-O3B	2.0915(7)	2.095	2.099	1.993(4)
*M*2-O1A	2.0182(7)	2.014	2.022	2.050(4)
*M*2-O1B	2.0224(7)	2.033	2.046	2.047(4)
*M*2-O2A	1.9324(7)	1.927	1.941	1.946(4)
*M*2-O2B	1.9427(7)	1.945	1.949	1.945(4)
*M*2-O4A	1.8293(7)	1.832	1.831	1.827(4)
*M*2-O4B	1.8387(7)	1.838	1.843	1.824(5)
*M*3-O1A x2	2.1048(7)	2.112	2.115	2.076(4)
*M*3-O1B x2	2.1108(6)	2.109	2.117	2.086(4)
*M*3-O3A	2.0727(10)	2.080	2.088	2.028(7)
*M*3-O3B	2.0756(10)	2.076	2.077	2.023(7)
*M*4-O2A	2.123(2)	2.142	2.193	2.157(10)
*M*4-O2B	2.109(2)	2.111	2.159	2.094(10)
*M*4-O4A	2.129(2)	2.153	2.156	2.176(10)
*M*4-O4B	2.074(2)	2.091	2.127	2.094(10)
*M*4-O5A	2.294(2)	2.342	2.321	2.309(9)
*M*4-O5B	2.896(2)	2.943	2.942	2.852(10)
*M*4-O6B	2.722(2)	2.686	2.616	2.674(10)
O3A-H1	0.80(3)	0.78(10)	0.7(2)	-
O3B-H2	0.75(3)	0.74(9)	0.62(12)	-
*M*1-*M*2	3.0752(4)	3.079(2)	3.086(2)	3.121(2)
*M*1-*M*2'	3.0869(4)	3.096(2)	3.106(2)	3.129(2)
O5A-O6A-O5A	166.77(5)	167.6(2)	168.8(2)	167.6(2)
O5B-O6B-O5B	164.02(4)	166.5(2)	168.9(3)	164.6(2)
*T*1A-O7A-*T*1A	147.56(7)	148.1(3)	149.0(4)	145.7(4)
*T*1B-O7B-*T*1B	146.51(8)	147.8(3)	148.4(4)	144.4(4)

Symmetry code: ' = *x*, *y*, 1+*z*.

Table 6. Refined site-scattering values (*epfu*) at the *M* sites in the Fe-rich holmquistite 3380B n. 7 and its partially deprotonated counterpart as a function of *T*.

T (K)	*M*1	*M*2	*M*3	∑C	*M*4(B)	∑(B+C)
298	35.44(6)	28.04(5)	18.97(2)	82.45	6.70(5)	89.15
523	34.84(17)	27.74(13)	18.75(6)	81.33	6.44(16)	87.77
773	35.42(20)	28.52(16)	18.30(6)	82.24	7.06(20)	89.30
298R*	36.26(22)	30.20(18)	15.07(7)	81.53	7.34(20)	88.87

* Collected at the end of the reversal experiment

Table 7. The site populations calculated for the B and C cations and W anions in Fe-rich holmquistite crystal 3380B n. 7 before (298 K) and after (298 KR) the annealing cycle. See text for more detail.

	Site population (*apfu*)	ss (*epfu*)		mbl (Å)	
		refined	calculated	refined	calculated*
298 K					
*M*1	1.18 Mg + 0.80 Fe^{2+} + 0.02 Mn^{2+}	35.44	35.46	2.096	2.098
*M*2	0.12 Fe^{2+} + 1.88 Al	28.04	27.56	1.931	1.937
*M*3	0.50 Mg + 0.50 Fe^{2+}	18.97	19.00	2.097	2.101
Σ C cations		82.45	82.02		
B cations	1.88 Li + 0.02 Na + 0.10 Mg^{2+}	6.70	7.06	2.335	
Σ (B+C) cations		89.15	89.08		
W anions	1.97 $(OH)^-$ + 0.03 F^-		*M*1-*M*2	3.087, 3.075	
298 KR					
*M*1	1.10 Mg + 0.85 Fe^{3+} + 0.03 Fe^{2+} + 0.02 Mn^{2+}	36.26	36.58	2.060	2.057
*M*2	0.30 Fe^{2+} + 1.70 Al	30.20	29.90	1.940	1.955
*M*3	0.53 Mg + 0.24 Fe^{2+} + 0.18 Al + 0.05 Li	15.07	15.09	2.063	2.063
Σ C cations		81.53	81.57		
B cations	1.83 Li + 0.02 Na + 0.15 Mg^{2+}	7.34	7.69	2.337	
Σ (B+C) cations		88.87	89.26		
W anions**	0.85 O^{2-} + 1.12 $(OH)^-$ + 0.03 F		*M*1-*M*2	3.129, 3.121	

* Calculated based on the <cation-O> distances modelled for monoclinic amphiboles

** The oxo component has been calculated based on the difference between the refined *M*1-*M*2 distances (cf. text for more detail)

Table 8. Comparison of the thermal volume expansivities of individual polyhedra ($\times 10^{-5}$ K^{-1}) measured for the three orthorhombic amphiboles of petrological relevance. Fe-rich Hol (this work); Ath = anthophyllite (Welch et al. 2011); Ged = gedrite (Zema et al. 2012). R = reversal experiments on the partially deprotonated phase. Site nomenclature after Hawthorne et al. (2012), mineral abbreviations according to Whitney and Evans (2010)**.**

Sample	*M*1	*M*2	*M*3	*M*4
Fe-rich Hol	2.65(2)	1.8(16)	2.0(5)	5.7(3)
Ath	4.4(1)	4.6(3)	4.09(3)	7.0(2)
Ged	4.6(3)	4.4(4)	4.94(7)	5.8(3)
Ged R	5.4(5)	2.3(5)	5.3(9)	7.1(3)

This is a preprint, the final version is subject to change, of the American Mineralogist (MSA)
Cite as Authors (Year) Title. American Mineralogist, in press.
DOI: https://doi.org/10.2138/am-2019-6966

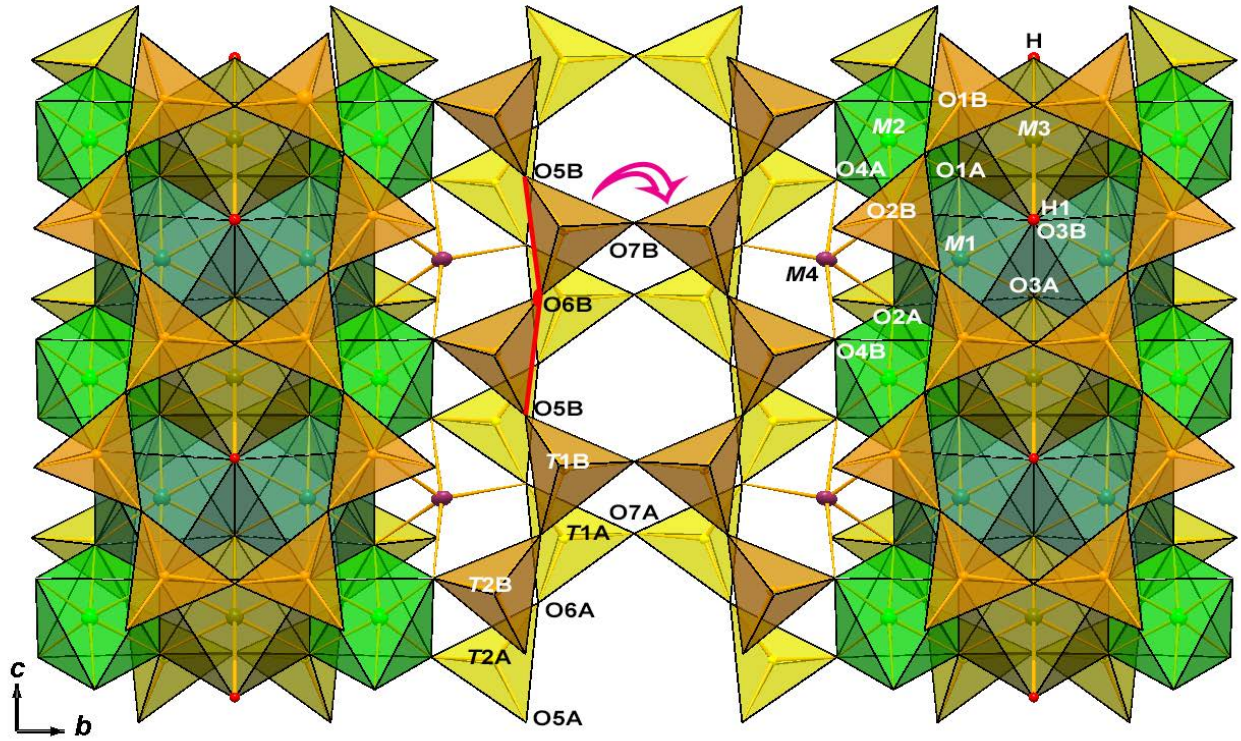

FIGURE 1. The crystal structure of Fe-rich holmquistite 3380B n.7 at R*T* projected onto (100). The relevant site nomenclature is shown according to Hawthorne and Oberti (2007). The red line indicates the kinking angle (O5-O6-O5), and the purple arrow the bowing angle (*T*1-O7-*T*1) for the B double-chain of tetrahedra.

This is a preprint, the final version is subject to change, of the American Mineralogist (MSA)
Cite as Authors (Year) Title. American Mineralogist, in press.
DOI: https://doi.org/10.2138/am-2019-6966

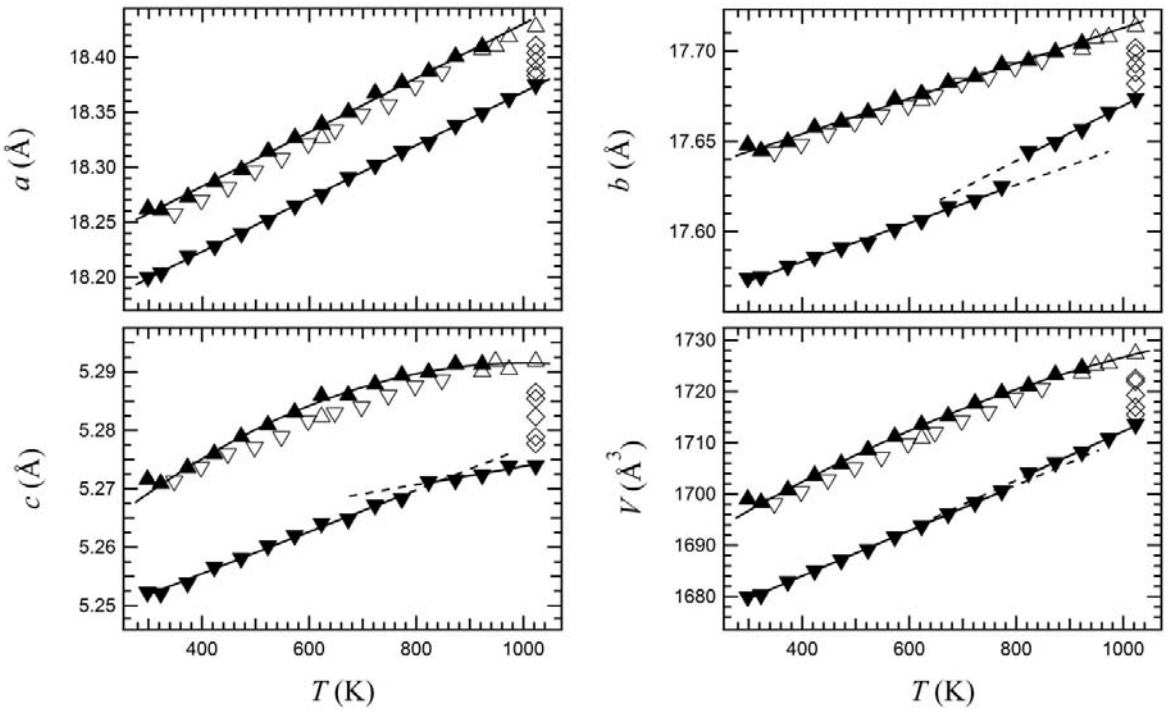

FIGURE 2. Changes in unit-cell parameters measured for Fe-rich holmquistite 3380B n. 7 during thermal annealing. All events recorded are reported in the graph: first heating to 923K (upward solid triangles); cooling to R*T* (downward empty triangles); re-heating up to 1023K (empty upward triangles); isothermal annealing at 1023K for 160 h (empty diamonds) showing contraction of all parameters due to the occurring of the deprotonation process; final cooling to R*T* of the deprotonated crystal (downward solid triangles).

This is a preprint, the final version is subject to change, of the American Mineralogist (MSA)
Cite as Authors (Year) Title. American Mineralogist, in press.
DOI: https://doi.org/10.2138/am-2019-6966

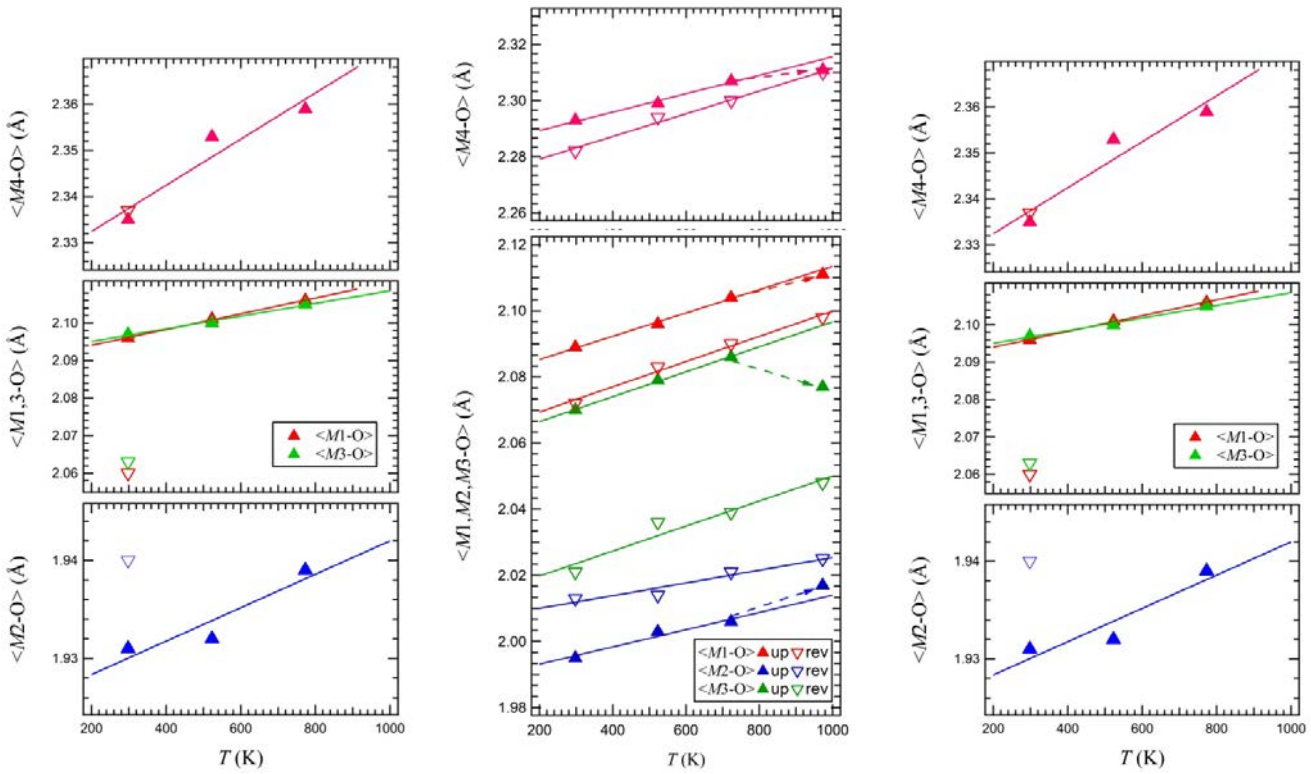

FIGURE 3. Changes in mean bond-lengths (corrected by riding motion) at the *M*1-3 octahedra and at the *M*4 [6+2] coordinated site observed during annealing in anthophyllite (left), gedrite (middle) and Fe-rich holmquistite 3380 n. 7 (right). Solid symbols: the original crystal; empty symbols: the deprotonated crystal.

This is a preprint, the final version is subject to change, of the American Mineralogist (MSA)
Cite as Authors (Year) Title. American Mineralogist, in press.
DOI: https://doi.org/10.2138/am-2019-6966

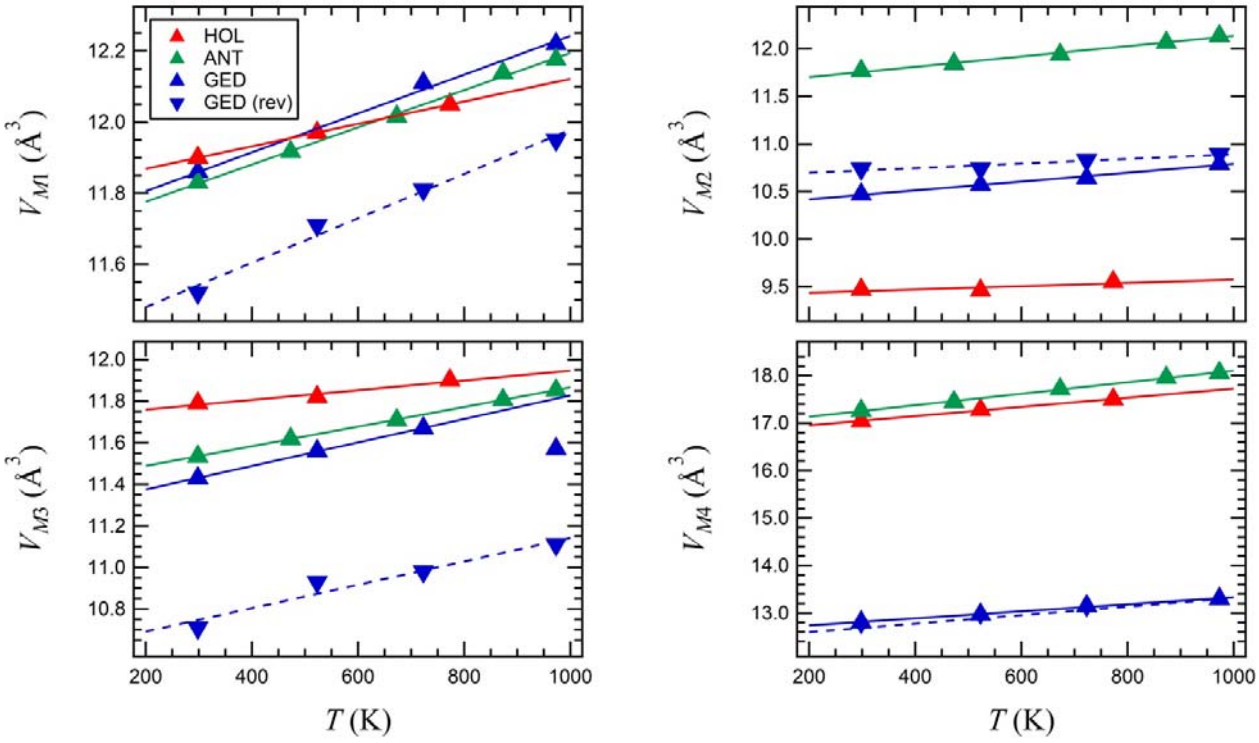

FIGURE 4. The evolution of the volumes of the individual polyhedra in holmquistite and in the other orthorhombic amphiboles studied so far. The calculated thermal expansivities are reported and compared in Table 8.

This is a preprint, the final version is subject to change, of the American Mineralogist (MSA)
Cite as Authors (Year) Title. American Mineralogist, in press.
DOI: https://doi.org/10.2138/am-2019-6966

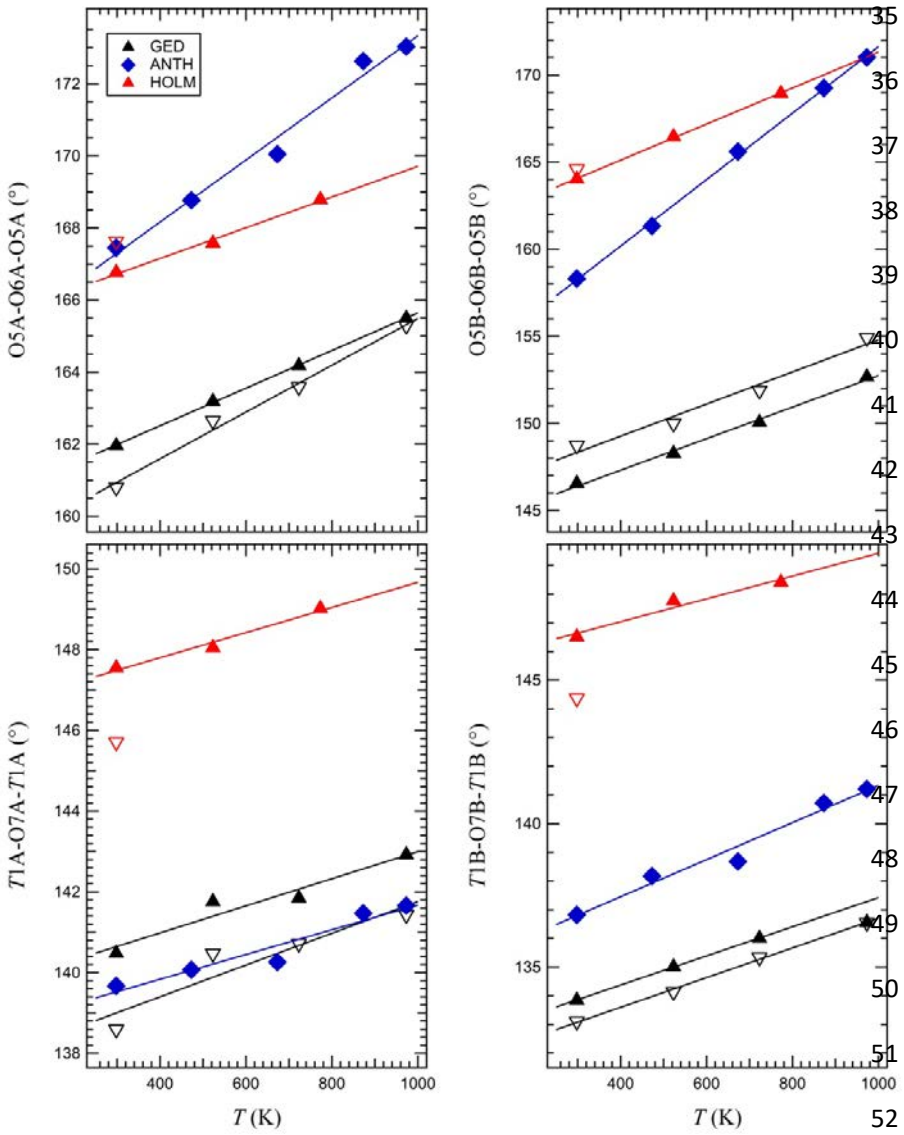

FIGURE 5. Changes in the kinking (O5-O6-O5) and bowing (*T*1-O7-*T*1) angles in the two independent double chains of tetrahedra (A and B) measured in orthorhombic amphiboles during thermal annealing. Solid symbols: the original crystal; empty symbols: the deprotonated crystal.